
Xiong, Xunhui; Zhao, Bote; Ding, Dong; Chen, Dongchang; Yang, Chenghao; Lei, Yong; Liu, Meilin:

One-step synthesis of architectural Ni₃S₂ nanosheet-on-nanorods array for use as high-performance electrodes for supercapacitors

Original published in:

NPG Asia Materials. - [London] : Macmillan Publishers Limited, part of Springer Nature. - 8 (2016), art. e300, 7 pp.

Original published: August 26, 2016

ISSN: 1884-4057

DOI: [10.1038/am.2016.126](https://doi.org/10.1038/am.2016.126)

[Visited: May 18, 2019]



This work is licensed under a [Creative Commons Attribution 4.0 International license](https://creativecommons.org/licenses/by/4.0/).

To view a copy of this license, visit

http://creativecommons.org/licenses/by/4.0

ORIGINAL ARTICLE

One-step synthesis of architectural Ni₃S₂ nanosheet-on-nanorods array for use as high-performance electrodes for supercapacitors

Xunhui Xiong^{1,2}, Bote Zhao², Dong Ding², Dongchang Chen², Chenghao Yang¹, Yong Lei³ and Meilin Liu²

Although a wide variety of three-dimensional porous electrode architectures have been created for supercapacitors to markedly enhance the charge and mass transfer associated with cycling, their low volumetric energy densities limit applications in many energy storage systems. In this work, we report a unique electrode architecture consisting of Ni₃S₂ nanosheet-onto-Ni₃S₂-nanorods grown on nickel foam and prepared using a simple one-step hydrothermal method. When tested as an electrode for a supercapacitor (using a three-electrode configuration), this material exhibited excellent rate capability and cycling stability at high cycling rates. The obtainable capacitance decreased by <42% as the current density was increased from 20 to 240 mA cm⁻², and the capacity retained 89.3% of its initial value after 5000 cycles at a cycling rate of 120 mA cm⁻². Further, an asymmetric supercapacitor consisting of the Ni₃S₂ nanosheet-onto-Ni₃S₂-nanorods electrode and an activated carbon (AC) electrode displayed a volumetric energy density as high as ~1.96 mWh cm⁻³, with the potential to bridge the performance gap between thin-film Li batteries and commercial AC//AC supercapacitors. The outstanding electrochemical performance is attributed to the good mechanical adhesion and electrical connection with the substrate, high contact area with the electrolyte and alleviated structural pulverization during the ion insertion/desertion process. It is predicted that the architectural Ni₃S₂-nanosheet-on-nanorods array prepared with this facile method offers great potential promise in large-scale energy storage device applications.

NPG Asia Materials (2016) 8, e300; doi:10.1038/am.2016.126; published online 26 August 2016

INTRODUCTION

The demand for clean energy and emerging ecological concerns have greatly stimulated research on the development of new, low-cost and environmentally friendly energy conversion and storage systems. To this end, supercapacitors have attracted much interest in the past decades because they can supply high power density and long cycle life. However, a major shortcoming of the existing supercapacitors is their low energy density (typically 5–10 Wh kg⁻¹), which is significantly lower than that of lithium ion batteries (120–180 Wh kg⁻¹).^{1–4} Higher energy density ($E = 0.5 CV^2$) can be achieved by increasing the cell voltage (V) and the specific or volumetric capacitance (C).^{5–7} In general, the cell voltage and the specific capacitance are determined primarily by electrode properties, such as composition, structure, morphology, particle size and porosity, among others.³ In addition to exploration of new electrode materials, much effort related to improved energy density of supercapacitors has been directed toward construction of novel architectures for full utilization of active electrode materials.

Typically, the highest capacitance of electrochemical double-layer capacitors on the basis of carbon-based materials is ~200 F g⁻¹.^{4,8–10} Transition metal oxides, hydroxides and sulfides have been demonstrated as alternative electrode materials with significantly enhanced capacity via surface-bound capacitor-like (that is, pseudo-capacitives) faradaic reactions.^{11–21} Ni- or/and Co-based oxides/hydroxides/sulfide usually exhibit a main capacitive behavior, especially at high current density, but the bulk materials still exhibit battery-type behavior. Therefore, these materials are considered as ‘extrinsic pseudo-capacitors.’ Among these extrinsic pseudo-active materials, metal sulfides have recently emerged as a more promising class of active materials owing to an electronic conductivity greater than that of the corresponding metal oxides or hydroxides.^{20,22} To further improve the utilization of metal sulfides, various nanostructures have been directly grown on three-dimensional porous current collectors to create high surface areas, short electron- and ion-transport pathways (which are required for high capacitance),^{19,23–28} and excellent rate capability and cycle performance. Xiao *et al.*¹⁹ reported on the preparation of highly

¹New Energy Research Institute, School of Environment and Energy, South China University of Technology, Guangzhou, China; ²School of Materials Science and Engineering, Georgia Institute of Technology, Atlanta, GA, USA and ³Institute of Physics and IMN MacroNano (ZIK), Ilmenau University of Technology, Ilmenau, Germany

Correspondence: Professor C Yang, New Energy Research Institute, School of Environment and Energy, South China University of Technology, Guangzhou, Guangdong 510006, China.

E-mail: esyangc@scut.edu.cn

or Professor M Liu, School of Materials Science and Engineering, Georgia Institute of Technology, 771 Ferst Drive, Atlanta, GA 30332-0245, USA.

E-mail: meilin.liu@mse.gatech.edu

Received 12 July 2015; revised 5 May 2016; accepted 26 June 2016

conductive NiCo₂S₄ crystalline nanotube arrays grown on carbon fiber papers using a hydrothermal process, thermal treatments and acid etching processes. The as-synthesized NiCo₂S₄ nanotube arrays showed a high areal capacitance of 0.87 F cm⁻² at 4 mA cm⁻². Chen *et al.* and Pu *et al.*^{25,26} prepared NiCo₂S₄ nanotubes on nickel foam using a multistep hydrothermal method that converted the corresponding nickel cobalt carbonate hydroxide precursors via S²⁻ ion exchange. Shen *et al.*¹⁸ reported a similar multistep route to growth of NiCo₂S₄ nanotube arrays on nitrogen-doped carbon foams. The NiCo₂S₄ electrode exhibited a capacitance of 877 F g⁻¹ at 20 A g⁻¹. Despite the attractive performance, the aforementioned methods involve multistep processes that make the development of the metal sulfides costly and complicated. Furthermore, supercapacitors on the basis of three-dimensional architecture have notably low volumetric energy densities owing to the large volume of the three-dimensional architecture and low loading amounts of electroactive materials.

In this work, we report an asymmetric supercapacitor consisting of a Ni₃S₂ nanosheet-onto-Ni₃S₂-nanorods (denoted as Ni₃S₂ nanosheet@nanorods) electrode and an activated carbon (AC) electrode. This asymmetric capacitor delivered a maximum volumetric energy density of ~1.96 mWh cm⁻³, potentially bridging the performance gap between thin-film Li batteries and commercial supercapacitors (on the basis of AC). Moreover, the Ni₃S₂ nanosheet@nanorods material was prepared using a simple one-step hydrothermal method, and the Ni₃S₂ nanorods and Ni₃S₂ multi-connected nanorods can also be obtained by varying the temperature of the hydrothermal process. Owing to the characteristics of greater contact area with the electrolyte and alleviated structural pulverization during the ion insertion/desertion process, Ni₃S₂ nanosheet@nanorods demonstrated the best rate capability and reversibility among these

three types of Ni₃S₂ nanostructures when tested in a three-electrode configuration.

MATERIALS AND METHODS

Materials synthesis

All reagents used in the experiments were of analytical grade and used without further purification. Ni₃S₂ nanoarrays were prepared using a simple one-step hydrothermal process. In brief, Ni foam (3 cm × 2.5 cm in a rectangular shape) was cleaned for several minutes with 3 M HCl solution, ethanol and deionized water under ultrasonic assistance. The Ni foam was placed against the wall of a 40 ml Teflon-lined stainless steel autoclave containing a 30 g homogeneous solution of 0.8 mmol Na₂S₂O₃. The autoclave was sealed, and the hydrothermal reaction was conducted at 115, 140 and 165 °C for 8 h to obtain Ni₃S₂ nanoarrays with different morphologies. After the autoclave was cooled to room temperature, the samples were rinsed with distilled water and dried in vacuum at 80 °C for 24 h.

Characterization

The phases of the samples were examined using X-ray diffraction analysis (PAN'alytical X'Pert Alpha 1 (Worcester, MA, USA) using Cu K-α1 X-rays). The microstructure and morphology were examined using scanning electron microscopy (SEM); (LEO 1530 field emission SEM, Zeiss, Germany) and high-resolution transmission electron microscopy (JEOL 4000 EX, Tokyo, Japan).

Electrochemical characterization

Electrochemical measurements were collected in a three-electrode electrochemical cell containing a 2 M KOH aqueous solution as the electrolyte at room temperature. The Ni₃S₂ nanoarray on Ni foam (1 cm²) was used as the working electrode. A platinum mesh (1.0 cm²) and an Ag/AgCl in saturated KCl electrode were used as the counter and the reference electrodes, respectively. On average, the mass loading of Ni₃S₂ nanostructures on Ni foam was determined by careful weighing after hydrothermal and drying processes. These values were ~4.4, 5.8 and 8.2 mg cm⁻² for Ni₃S₂ prepared at 115, 140

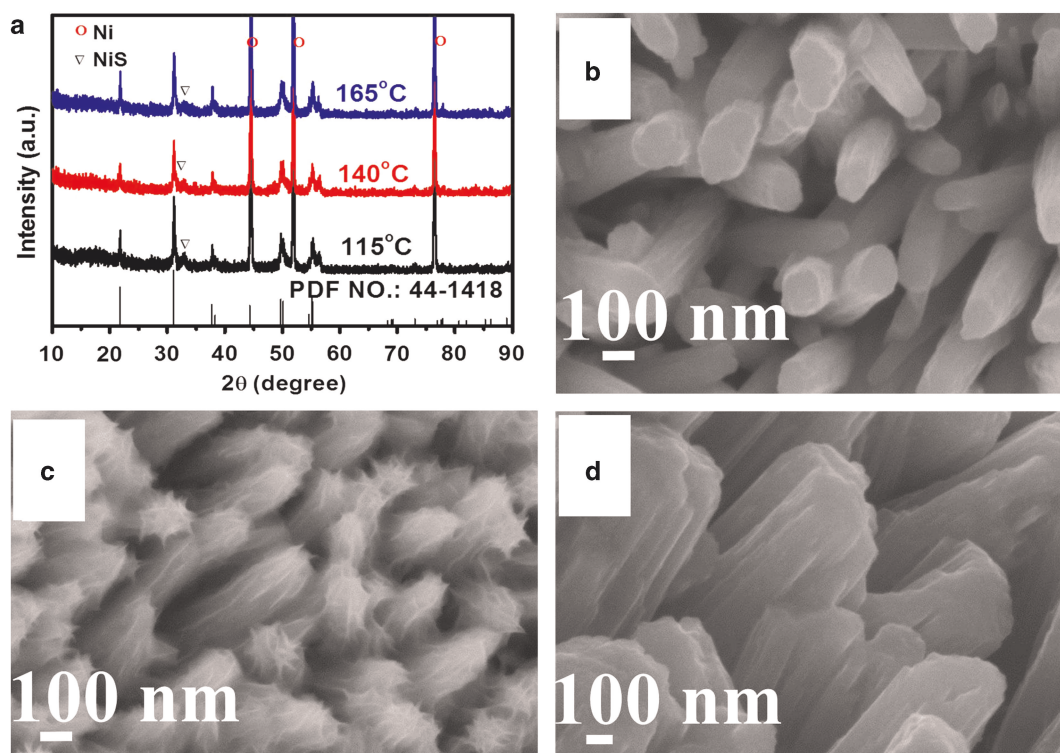


Figure 1 XRD patterns (a) and SEM images of the obtained Ni₃S₂ prepared at different temperatures: (b) 115 °C, (c) 140 °C and (d) 165 °C. SEM, scanning electron microscopy; XRD, X-ray diffraction.

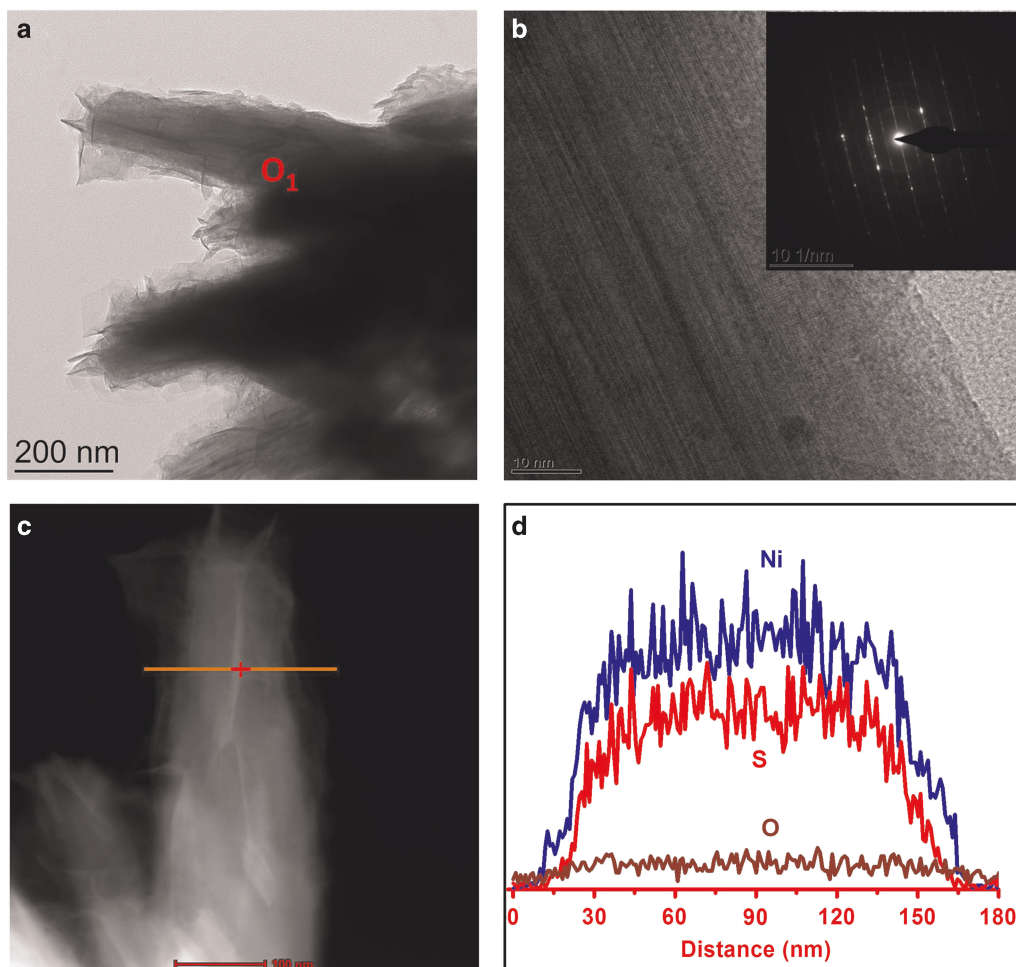


Figure 2 TEM image (a) and HRTEM images (b) of Ni₃S₂ nanosheet@nanorods, (c) HAADF-STEM image of an individual Ni₃S₂ nanosheet@nanorod and (d) linear scanning results of the highlighted area. HAADF, high-angle annular dark-field; HRTEM, high-resolution TEM; STEM, scanning TEM; TEM, transmission electron microscopy.

and 165 °C, respectively (see detailed calculation in Supplementary Table S1). Before use, the nickel foam was compacted at 50 MPa. Cyclic voltammograms were acquired in a potential range from -0.2 to 0.7 V vs REF at different scan rates, and the cyclic stability was evaluated by galvanostatic charge-discharge measurements from -0.1 to 0.55 V vs REF at a current density of 120 mA cm⁻² for 5000 cycles.

Electrochemical measurements of the asymmetric supercapacitor were conducted to evaluate the Ni₃S₂ nanosheet@Ni₃S₂ nanorods for practical application in a two-electrode cell in a 2 M KOH aqueous electrolyte solution. The Ni₃S₂ nanosheet@Ni₃S₂ nanorods material was used directly as the positive electrode, and the AC film served as the negative electrode. The AC film was first prepared by mixing 90 wt% AC and 10 wt% PTFE to form a paste that was subsequently rolled into uniform sheet. All electrochemical measurements were conducted using a Solartron SI 1286 electrochemical workstation (Leicester, UK).

RESULTS AND DISCUSSION

Ni₃S₂ nanostructures were prepared using a facile one-step hydrothermal process. During the hydrothermal process, the active species (S ions) released from Na₂S₂O₃ react with Ni to form Ni₃S₂ nanostructures on the surface of the Ni foam. The X-ray diffraction patterns of the as-prepared Ni₃S₂ nanostructured arrays are shown in Figure 1a. The three strong peaks at 2θ = 44.7, 52.1 and 76.6 arise from the Ni foam substrate. The diffraction peaks at 2θ = 21.8, 31.1, 37.8, 38.3, 49.9, 50.2, 54.6 and 55.1°, respectively, correspond to the

(101), (110), (003), (021), (113), (211), (104) and (122) planes of Ni₃S₂ (JCPDS no. 44-1418). A notably small amount of NiS (Supplementary Figure S1) is also observed in the X-ray diffraction pattern, which was also frequently observed when Ni foam was used as a template and/or Ni source to prepare Ni₃S₂ using a one-step *in situ* growth method.^{27,29} All samples prepared at different temperatures displayed the same structure, as also confirmed by Raman spectroscopy (Supplementary Figure S2).

The morphological details of the as-obtained Ni₃S₂ were examined using field emission SEM. Figure 1 shows the SEM images of the obtained Ni₃S₂ prepared at different temperatures. The Ni₃S₂ sample prepared at 115 °C exhibited nanorod arrays with a smooth surface and a length of 1–1.2 μm (Figure 1b and Supplementary Figure S3a). When the temperature was increased to 145 °C, the smooth surface became rough and was decorated by many tiny ‘buds,’ as shown in Figure 1c. This unique feature was further examined under transmission electron microscopy (TEM) equipped with energy-dispersive X-ray spectrometry. Figure 2a shows a typical TEM image of an individual nanostructure in which the Ni₃S₂ nanorods are uniformly wrapped by ultrathin nanosheets. The energy-dispersive X-ray spectrometry results (Supplementary Figure S4) from the selected point in Figure 2a clearly show that the strongest signals for Ni and S were found in the backbone region. The trace amount of O element

might originate from the hydroxyl group at the edge of nanosheet. The high-resolution TEM image and the corresponding selected-area electron diffraction patterns in Figure 2b demonstrate that the Ni₃S₂ has a twin-crystalline structure. The high-angle annular dark-field scanning TEM image in Figure 2c shows the ultrathin characteristic of the Ni₃S₂ on the surface more clearly. The composition of individual Ni₃S₂ nanosheet@nanorods was confirmed by the linear scanning results (Figure 2d), which are consistent with the earlier energy-dispersive X-ray spectrometry result. As the temperature was increased

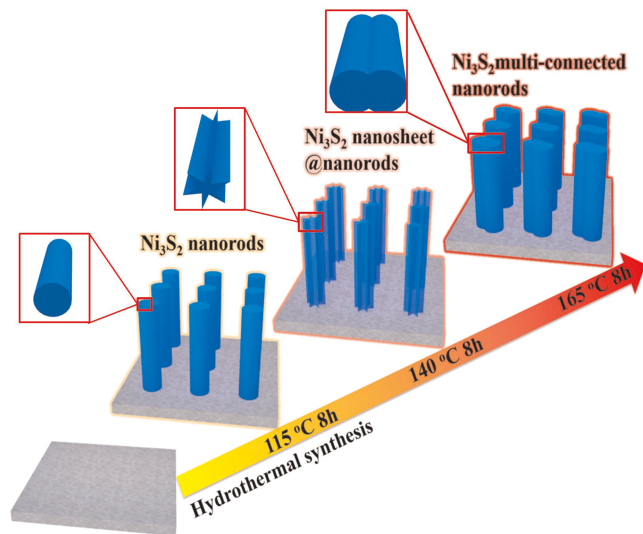
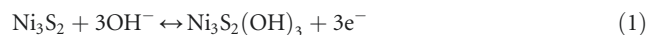


Figure 3 Schematic illustration of the proposed mechanism for the growth of Ni₃S₂ nanosheet@nanorods.

to 165 °C, the morphology of the sample changed significantly, and it appeared that several nanorods bonded together (Figure 1d). When the temperature was further increased, the nanorods nearly disappeared and the Ni foam was covered with a dense Ni₃S₂ layer (Supplementary Figure S5e and f).

A possible growth mechanism for the different morphology of Ni₃S₂ is proposed on the basis of these experimental results (Figure 3). During the hydrothermal process, the active species (S ions) released from Na₂S₂O₃ react with Ni foam to form Ni₃S₂ nanorods on the surface after holding at 115 °C for 0.5 h (Supplementary Figure S5a and b), and many relatively short nanorods grow on the Ni foam. The longer reaction time is necessary to grow additional Ni₃S₂ nanorods, but no obvious changes were noted as the time was extended from 8 to 16 h (Supplementary Figure S5c and d). If the reaction temperature is increased to 145 °C, the Ni₃S₂ nanorods are etched by hydrothermal steaming, resulting in an open porous structure with ultrathin Ni₃S₂ nanosheets uniformly wrapped on the nanorod surface. At even higher temperatures (>165 °C), the nanorods bond together, driven by minimization of surface energy of the system.

Figure 4a shows the CV curves of Ni₃S₂ nanorod arrays obtained at different temperatures. All CV curves exhibit a pronounced pair of redox peaks in the potential range from -0.2 to 0.7 V. According to previous studies of the electrochemical properties of nickel sulfide in a KOH solution, the redox peaks at near 0.48 and 0.12 V (vs Ag/AgCl) can be attributed to the reversible redox reactions of Ni²⁺/Ni³⁺ as shown below.



The specific capacitances of the three types of Ni₃S₂ calculated from the CV curves at 30 mV s⁻¹ are 420, 464 and 306 F g⁻¹, respectively

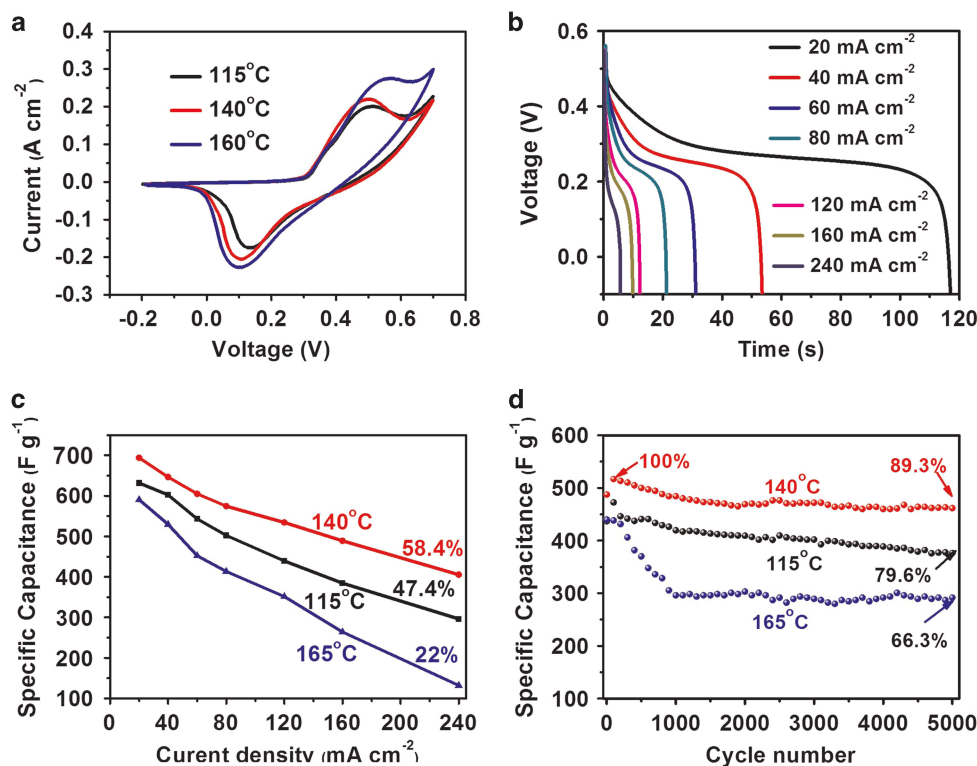


Figure 4 Cyclic voltammograms of (a) Ni₃S₂ obtained at different temperatures at a scan rate of 30 mV s⁻¹ and (b) Ni₃S₂ nanosheet@Ni₃S₂ nanorods electrode at different scan rates from 30 to 80 mV s⁻¹ in a voltage window of -0.2 to 0.7 V. (c) Constant current discharge curves of Ni₃S₂ nanosheet@Ni₃S₂ nanorods electrode at different current densities. (d) Specific capacitances at different current densities.

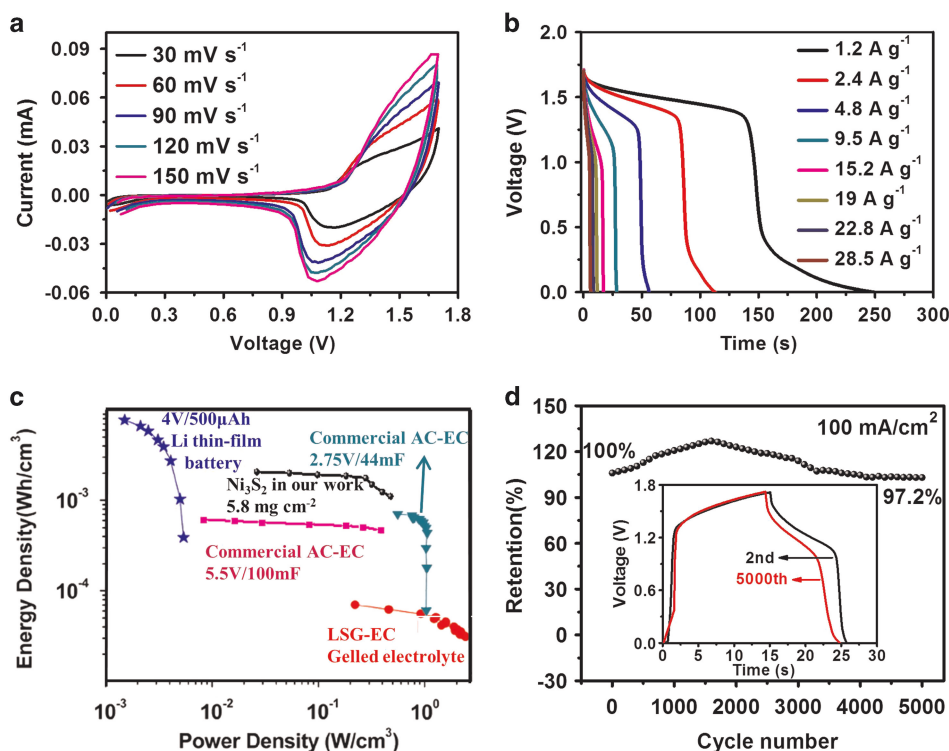


Figure 5 CV (a) and discharge curves (b) of the asymmetric supercapacitor. (c) Volumetric energy densities of our supercapacitor compared with other data. Data for laser-scribed graphene (LSG) supercapacitor, Li thin-film battery and commercial AC//AC supercapacitor are reproduced from El-Kady *et al.*³⁴ (d) Cycling stability of our device. AC, activated carbon; C, capacitance; EC, electrochemical capacitors; V, voltage.

(detailed calculations can be found in the Supplementary Information), showing that Ni₃S₂ nanosheet@nanorods display the highest specific capacitance. From the relationship between the anodic peak current (i_p) and scan rate (ν) shown in Supplementary Figure S6d, it can be observed that the rate of the redox reaction of the Ni₃S₂ electrode is limited by diffusion. Thus, properties of the electrode such as interface/surface structure and ionic/electronic diffusion have vital roles in enhancing the rate capability and the specific capacitance of the supercapacitors (Supplementary Figure S7). The high specific capacitance of Ni₃S₂ nanosheet@nanorods can be ascribed to the high BET surface area (Supplementary Figure S8), which is highly beneficial for transport and diffusion of electrolyte ions during the charge–discharge cycling of supercapacitors. In comparison, screening effects between the nanorod arrays occurred for Ni₃S₂ multi-connected nanorods, which decrease the specific surface area and thus decrease the specific capacitance. Furthermore, the sample with screening effects does not have sufficient space to buffer the volume changes during the charging/discharging process, thus leading to poor cycle performance. Figure 4b shows the charge/discharge voltage profiles at current densities from 20 to 240 mA cm⁻² in the voltage window from -0.1 to 0.55 V. The specific capacitances (F g⁻¹) under galvanostatic conditions were calculated from the formula below:^{13,30,31}

$$C = \frac{2i_m \int V dt}{V^2|_{V_i}} \quad (2)$$

where $i_m = I/m$ (A g⁻¹) is the current density, I is the current, m is the active mass of the electrode, and V is the potential with an initial and final value of V_i and V_f , respectively. The calculated specific capacitances as a function of the discharge current density are presented in Figure 4c. The Ni₃S₂ nanosheet@nanorods displays the

highest specific capacitance of 694 F g⁻¹ at a discharge current density of 20 mA cm⁻² (3.45 A g⁻¹); (the current density and specific capacitance were normalized on the basis of mass of the Ni₃S₂ and a voltage of 0.65 V). The specific capacitance gradually decreases with the increment in current density owing to mass transport limitations. However, this material still showed notably high-rate stability. The specific capacitance decreased by <42% as the current density was increased from 20 to 240 mA cm⁻², which is much higher than that of the Ni₃S₂ nanorods and the Ni₃S₂ multi-connected nanorods. The effect of the electrode properties is also demonstrated by the difference in cycling performance. As shown in Figure 4d, the capacitance of Ni₃S₂ multi-connected nanorods fades rapidly, from 439.6 F g⁻¹ for the first cycle to 292.3 F g⁻¹ for the 1000th cycle, corresponding to ~66.5% retention after 1000 cycles. No further degradation occurred in subsequent cycles. The Ni₃S₂ nanorods and Ni₃S₂ nanosheet@nanorods also showed a certain amount of degradation for the first several hundred cycles and remained relatively stable in the subsequent cycles. However, these materials showed significantly enhanced cycling stability, especially for the Ni₃S₂ nanosheet@nanorods, which showed an initial capacity of 489 F g⁻¹ and maintained 89.3% of their initial value after 5000 cycles. The high specific capacitance at large current density and the stability were rarely reported in previous studies (Supplementary Table S2).

To validate these results, we performed SEM analysis of the Ni₃S₂ electrode after 5000 cycles (Supplementary Figures S9 and S10), and it was clear that significant changes occurred in the morphology for all samples. For the Ni₃S₂ nanorods and Ni₃S₂ multi-connected nanorods, the capacitance loss is likely owing to delamination of the materials from the substrate caused by the volume change during the ion insertion/desertion process. The delamination was significantly alleviated for the Ni₃S₂ nanosheets@nanorods. In this configuration,

the Ni₃S₂ nanorods are well wrapped by Ni₃S₂ nanosheets, and the highly open structure offers sufficient space to buffer the volume changes during the charging/discharging process. At the same time, Ni₃S₂ nanosheets largely increase the contact areas between the electrolyte and active materials, and greatly facilitate ion and electron diffusion. More interestingly, the nanorods were replaced by Ni₃S₂ nanoflakes (Supplementary Figures S10b and S11) with formation of nickel hydroxides (Supplementary Figure S10c) on the surface in the alkaline solution. With a highly porous cross-linked structure, the Ni₃S₂ nanoflakes allow rapid electron conduction and electrolyte ionic diffusion, which greatly largely contribute to the excellent cycle performance at large current densities. This outstanding long-term electrochemical stability was further confirmed by cycling at a higher current density (240 mA cm⁻² or 41.4 A g⁻¹), as is further evident from the notably stable charge-discharge curves for the first 5 cycles and the last 5 cycles, with 99.1% Coulombic efficiency. At such a high current density, a specific capacitance of 306.2 F g⁻¹ (81.8% of the highest value of 374.5 F g⁻¹) was still maintained after 16 000 cycles (Supplementary Figure S12).

To further evaluate the Ni₃S₂ nanosheet@Ni₃S₂ nanorods electrode for real applications, we assembled an asymmetric supercapacitor consisting of a Ni₃S₂ nanosheet@Ni₃S₂ nanorods electrode and an AC electrode separated by a glass fiber separator. One advantage of the asymmetric supercapacitor is the use of the pseudo-capacitive electrode to enhance the specific capacitance of the cell. However, the operating voltage of the asymmetric configuration can be extended to near 1.5–2 V owing to the overpotential of the reversible hydrogen electrosorption in a carbon-based negative electrode.^{7,32,33} After calculation on the basis of the specific capacitance of AC and Ni₃S₂ nanosheet@Ni₃S₂ nanorods obtained in a three-electrode electrochemical cell (Supplementary Figure S13), 10.7 mg of AC film was chosen to balance the capacitance of a piece of the electrode (0.32 cm²). Figure 5a shows the CV curves of an optimized asymmetric supercapacitor at various scan rates of 30, 60, 90, 120 and 150 mV s⁻¹, as measured between 0 and 1.7 V in 2 M KOH aqueous electrolyte. The CV curves show well-defined redox peaks in the range of 0–1.7 V, indicating only pseudo-capacitive capacitor behavior at all scan rates. Moreover, the cell voltage of the Ni₃S₂-AC-based asymmetric supercapacitor was increased to 1.7 V, which is almost twice that of conventional AC-based symmetric capacitors in aqueous electrolytes (0.8–1.0 V). The galvanostatic charge/discharge plots at different current densities with a potential window of 1.7 V are shown in Figure 5b. On the basis of these data, a Ragone plot of the device was obtained, as shown in Figure 5c. The energy and power densities (E and P) were calculated using equations:

$$E = \frac{I \int V dt}{T_{\text{cell}}} \quad (3)$$

$$P = \frac{E}{t} \quad (4)$$

where I is the charge–discharge current, $V(t)$ is the cell voltage, T_{cell} is the volume of the device (including current collector, anode, cathode, separator, device area of 1.26 cm² and total measured thickness of 0.75 cm) and t is the discharging time. Although the gravimetric energy density (Supplementary Figure S14) is largely limited by the low utilization efficiency of the electroactive material caused by the rarely reported high loading density (5.8 mg cm⁻²), a maximum volumetric energy density and power density of 1.96 mWh cm⁻³ at 1.2 A g⁻¹ and 0.6 W cm⁻³ at 28.3 A g⁻¹ are obtained, respectively. The volumetric power densities of our supercapacitor are further

shown in Figure 5c and are compared with previously reported data. It can be observed that the supercapacitor bridges the performance gap between 500 μAh thin-film Li batteries and electrochemical double-layer capacitors (laser-scribed graphene supercapacitor³⁴ and commercial AC supercapacitor). The demonstrated energy density is also greatly superior to those of most asymmetric supercapacitors on the basis of thin-film electrodes fabricated directly on carbon cloth, such as H-TiO₂@MnO₂//H-TiO₂@C (~0.3 mWh cm⁻³),³⁵ WO_{3-x}@MoO_{3-x}//PANI (~1.9 mWh cm⁻³),³⁶ Co₉S₈//Co₃O₄@RuO₂ (~1.21 mWh cm⁻³),³⁷ VO_x//VN (~0.61 mWh cm⁻³)³⁸ and MnO₂//Fe₂O₃ (~0.55 mWh cm⁻³).³⁹ Figure 5d reveals the outstanding cycling life of our supercapacitor after up to 5000 cycles. The capacitance increase during the first 1500 cycles is likely owing to an ‘activation process.’⁴⁰ After ~1500 cycles, the capacitance decreased gradually, most likely owing to structural changes associated with the redox reactions, which can be confirmed by the weight changes before and after cycling test (Supplementary Figure S10). However, the degradation in performance subsequently diminished owing to formation of Ni₃S₂ nanoflakes, which create sufficient space to buffer the volume changes.

CONCLUSION

In summary, the Ni₃S₂ nanosheet@nanorods material was prepared via a simple but efficient one-step hydrothermal process. By controlling the reaction temperature, we prepared three types of Ni₃S₂ nanostructures, namely, Ni₃S₂ nanorods, Ni₃S₂ nanosheet@nanorods and Ni₃S₂ multi-connected nanorods. The Ni₃S₂ nanosheet@nanorods demonstrated the highest specific capacitance of 694 F g⁻¹ at a discharge current density of 20 mA cm⁻² with excellent rate stability. The enhanced performance is attributed to the unique architecture of the Ni₃S₂ nanosheet, which has a high contact area with the electrolyte and alleviated structural pulverization during cycling. Our work not only offers the possibility of engineering nickel sulfide into a promising pseudo-capacitive material, but also presents a simple approach to design a new architecture for energy storage devices.

CONFLICT OF INTEREST

The authors declare no conflict of interest.

ACKNOWLEDGEMENTS

This work was supported by the US National Science Foundation under award number DMR-1410320, the Natural Science Foundation of China (51402109) and the Natural Science Foundation of Guangdong Province, China (S2013010014883).

Author contributions: XX, CY and ML formulated the project. XX prepared the electrode samples, and collected and analyzed the microstructural and electrochemical data. DD and BZ collected and analyzed the SEM and TEM image data. DC collected and analyzed the Raman data. XX wrote the paper and all authors contributed to revision of the paper.

- 1 Miller, J. R. & Simon, P. Materials science. Electrochemical capacitors for energy management. *Science* **321**, 651–652 (2008).
- 2 Simon, P. & Gogotsi, Y. Materials for electrochemical capacitors. *Nat. Mater.* **7**, 845–854 (2008).
- 3 Wang, G., Zhang, L. & Zhang, J. A review of electrode materials for electrochemical supercapacitors. *Chem. Soc. Rev.* **41**, 797–828 (2012).
- 4 Liu, C., Yu, Z., Neff, D., Zhamu, A. & Jang, B. Z. Graphene-based supercapacitor with an ultrahigh energy density. *Nano Lett.* **10**, 4863–4868 (2010).
- 5 Robertson, J. Realistic applications of CNTs. *Materials Today* **7**, 46–52 (2004).
- 6 Sung, J.-H., Kim, S.-J. & Lee, K.-H. Fabrication of microcapacitors using conducting polymer microelectrodes. *J. Power Sources* **124**, 343–350 (2003).

- 7 Yu, X., Lu, B. & Xu, Z. Super long-life supercapacitors based on the construction of nanohoneycomb-like strongly coupled CoMoO₄-3D graphene hybrid electrodes. *Adv. Mater.* **26**, 1044–1051 (2014).
- 8 Frackowiak, E. & Béguin, F. Carbon materials for the electrochemical storage of energy in capacitors. *Carbon* **39**, 937–950 (2001).
- 9 Wu, Z.-S., Zhou, G., Yin, L.-C., Ren, W., Li, F. & Cheng, H.-M. Graphene/metal oxide composite electrode materials for energy storage. *Nano Energy* **1**, 107–131 (2012).
- 10 Zhu, Y., Murali, S., Stoller, M. D., Ganesh, K. J., Cai, W., Ferreira, P. J., Pirkle, A., Wallace, R. M., Cychosz, K. A., Thommes, M., Su, D., Stach, E. A. & Ruoff, R. S. Carbon-based supercapacitors produced by activation of graphene. *Science* **332**, 1537–1541 (2011).
- 11 Yang, L., Cheng, S., Ding, Y., Zhu, X., Wang, Z. L. & Liu, M. Hierarchical network architectures of carbon fiber paper supported cobalt oxide nanonets for high-capacity pseudocapacitors. *Nano Lett.* **12**, 321–325 (2011).
- 12 Huang, L., Chen, D., Ding, Y., Feng, S., Wang, Z. L. & Liu, M. Nickel-cobalt hydroxide nanosheets coated on NiCo₂O₄ nanowires grown on carbon fiber paper for high-performance pseudocapacitors. *Nano Lett.* **13**, 3135–3139 (2013).
- 13 Xiong, X., Ding, D., Chen, D., Waller, G., Bu, Y., Wang, Z. & Liu, M. Three-dimensional ultrathin Ni(OH)₂ nanosheets grown on nickel foam for high-performance supercapacitors. *Nano Energy* **11**, 154–161 (2015).
- 14 Wei, W., Cui, X., Chen, W. & Ivey, D. G. Manganese oxide-based materials as electrochemical supercapacitor electrodes. *Chem. Soc. Rev.* **40**, 1697–1721 (2011).
- 15 Perera, S. D., Patel, B., Nijem, N., Roodenko, K., Seitz, O., Ferraris, J. P., Chabal, Y. J. & Balkus, K. J. Vanadium oxide nanowire-carbon nanotube binder-free flexible electrodes for supercapacitors. *Adv. Energy Mater.* **1**, 936–945 (2011).
- 16 Wang, B., Chen, J. S., Wang, Z., Madhavi, S. & Lou, X. W. Green synthesis of NiO nanobelts with exceptional pseudo-capacitive properties. *Adv. Energy Mater.* **2**, 1188–1192 (2012).
- 17 Rakhii, R. B., Chen, W., Cha, D. & Alshareef, H. N. Nanostructured ternary electrodes for energy-storage applications. *Adv. Energy Mater.* **2**, 381–389 (2012).
- 18 Shen, L., Wang, J., Xu, G., Li, H., Dou, H. & Zhang, X. NiCo₂S₄ nanosheets grown on nitrogen-doped carbon foams as an advanced electrode for supercapacitors. *Adv. Energy Mater.* **5**, 1400977 (2015).
- 19 Xiao, J., Wan, L., Yang, S., Xiao, F. & Wang, S. Design hierarchical electrodes with highly conductive NiCo₂S₄ nanotube arrays grown on carbon fiber paper for high-performance pseudocapacitors. *Nano Lett.* **14**, 831–838 (2014).
- 20 Chen, H., Jiang, J., Zhang, L., Wan, H., Qi, T. & Xia, D. Highly conductive NiCo₂S₄ urchin-like nanostructures for high-rate pseudocapacitors. *Nanoscale* **5**, 8879–8883 (2013).
- 21 Yu, L., Zhang, L., Wu, H. B. & Lou, X. W. Formation of Ni_xCo_{3-x}S₄ hollow nanoprisms with enhanced pseudocapacitive properties. *Angew. Chem. Int. Ed. Engl.* **53**, 3711–3714 (2014).
- 22 Xiao, J., Zeng, X., Chen, W., Xiao, F. & Wang, S. High electrocatalytic activity of self-standing hollow NiCo₂S₄ single crystalline nanorod arrays towards sulfide redox shuttles in quantum dot-sensitized solar cells. *Chem. Commun.* **49**, 11734–11736 (2013).
- 23 Chen, W., Xia, C. & Alshareef, H. N. One-step electrodeposited nickel cobalt sulfide nanosheet arrays for high-performance asymmetric supercapacitors. *ACS Nano* **8**, 9531–9541 (2014).
- 24 Xia, X., Zhu, C., Luo, J., Zeng, Z., Guan, C., Ng, C. F., Zhang, H. & Fan, H. J. Synthesis of free-standing metal sulfide nanoarrays via anion exchange reaction and their electrochemical energy storage application. *Small* **10**, 766–773 (2014).
- 25 Pu, J., Wang, T., Wang, H., Tong, Y., Lu, C., Kong, W. & Wang, Z. Direct growth of NiCo₂S₄ nanotube arrays on nickel foam as high-performance binder-free electrodes for supercapacitors. *Chempluschem.* **79**, 577–583 (2014).
- 26 Chen, H., Jiang, J., Zhang, L., Xia, D., Zhao, Y., Guo, D., Qi, T. & Wan, H. *In situ* growth of NiCo₂S₄ nanotube arrays on Ni foam for supercapacitors: maximizing utilization efficiency at high mass loading to achieve ultrahigh areal pseudocapacitance. *J. Power Sources* **254**, 249–257 (2014).
- 27 Zhou, W., Cao, X., Zeng, Z., Shi, W., Zhu, Y., Yan, Q., Liu, H., Wang, J. & Zhang, H. One-step synthesis of Ni₃S₂ nanorod@Ni(OH)₂ nanosheet core-shell nanostructures on a three-dimensional graphene network for high-performance supercapacitors. *Energy Environ. Sci.* **6**, 2216–2221 (2013).
- 28 Xiong, X., Waller, G., Ding, D., Chen, D., Rainwater, B., Zhao, B., Wang, Z. & Liu, M. Controlled synthesis of NiCo₂S₄ nanostructured arrays on carbon fiber paper for high-performance pseudocapacitors. *Nano Energy* **16**, 71–80 (2015).
- 29 Wei, W., Mi, L., Gao, Y., Zheng, Z., Chen, W. & Guan, X. Partial ion-exchange of nickel-sulfide-derived electrodes for high performance supercapacitors. *Chem. Mater.* **26**, 3418–3426 (2014).
- 30 Yang, P. & Mai, W. Flexible solid-state electrochemical supercapacitors. *Nano Energy* **8**, 274–290 (2014).
- 31 Mai, L. Q., Minhas-Khan, A., Tian, X., Hercule, K. M., Zhao, Y. L., Lin, X. & Xu, X. Synergistic interaction between redox-active electrolyte and binder-free functionalized carbon for ultrahigh supercapacitor performance. *Nat. Commun.* **4**, 2923 (2013).
- 32 Yan, J., Fan, Z., Sun, W., Ning, G., Wei, T., Zhang, Q., Zhang, R., Zhi, L. & Wei, F. Advanced asymmetric supercapacitors based on Ni(OH)₂/graphene and porous graphene electrodes with high energy density. *Adv. Funct. Mater.* **22**, 2632–2641 (2012).
- 33 Tang, Z., Tang, C.-h. & Gong, H. A high energy density asymmetric supercapacitor from nano-architected Ni(OH)₂/carbon nanotube electrodes. *Adv. Funct. Mater.* **22**, 1272–1278 (2012).
- 34 El-Kady, M. F., Strong, V., Dubin, S. & Kaner, R. B. Laser scribing of high-performance and flexible graphene-based electrochemical capacitors. *Science* **335**, 1326–1330 (2012).
- 35 Lu, X., Yu, M., Wang, G., Zhai, T., Xie, S., Ling, Y., Tong, Y. & Li, Y. H-TiO₂@MnO₂/H-TiO₂@C core-shell nanowires for high performance and flexible asymmetric supercapacitors. *Adv. Mater.* **25**, 267–272 (2013).
- 36 Xiao, X., Ding, T., Yuan, L., Shen, Y., Zhong, Q., Zhang, X., Cao, Y., Hu, B., Zhai, T., Gong, L., Chen, J., Tong, Y., Zhou, J. & Wang, Z. L. WO_{3-x}/MoO_{3-x} core/shell nanowires on carbon fabric as an anode for all-solid-state asymmetric supercapacitors. *Adv. Energy Mater.* **2**, 1328–1332 (2012).
- 37 Xu, J., Wang, Q., Wang, X., Xiang, Q., Liang, B., Chen, D. & Shen, G. Flexible asymmetric supercapacitors based upon Co₉S₈ nanorod/Co₃O₄@RuO₂ nanosheet arrays on carbon cloth. *ACS Nano* **7**, 5453–5462 (2013).
- 38 Lu, X., Yu, M., Zhai, T., Wang, G., Xie, S., Liu, T., Liang, C., Tong, Y. & Li, Y. High energy density asymmetric quasi-solid-state supercapacitor based on porous vanadium nitride nanowire anode. *Nano Lett.* **13**, 2628–2633 (2013).
- 39 Yang, P., Ding, Y., Lin, Z., Chen, Z., Li, Y., Qiang, P., Ebrahimi, M., Mai, W., Wong, C. P. & Wang, Z. L. Low-cost high-performance solid-state asymmetric supercapacitors based on MnO₂ nanowires and Fe₂O₃ nanotubes. *Nano Lett.* **14**, 731–736 (2014).
- 40 Ji, J., Zhang, L. L., Ji, H., Li, Y., Zhao, X., Bai, X., Fan, X., Zhang, F. & Ruoff, R. S. Nanoporous Ni(OH)₂ thin film on 3D ultrathin-graphite foam for asymmetric supercapacitor. *ACS Nano* **7**, 6237–6243 (2013).



This work is licensed under a Creative Commons Attribution 4.0 International License. The images or other third party material in this article are included in the article's Creative Commons license, unless indicated otherwise in the credit line; if the material is not included under the Creative Commons license, users will need to obtain permission from the license holder to reproduce the material. To view a copy of this license, visit <http://creativecommons.org/licenses/by/4.0/>

© The Author(s) 2016

Supplementary Information accompanies the paper on the NPG Asia Materials website (<http://www.nature.com/am>)